Interplay of seismic and aseismic deformations during earthquake swarms: an experimental approach

O. Lengliné[a,*], J. E. Elkhoury[b], G. Daniel[c], J. Schmittbuhl[a], R. Toussaint[a], J.-P. Ampuero[b], M. Bouchon[d]

[a] *Institut de Physique du Globe de Strasbourg, CNRS et Université de Strasbourg (EOST), France*
[b] *Seismological Laboratory, Caltech, Pasadena, USA*
[c] *Magnitude, Research and Development, Centre Regain, Sainte-Tulle, France*
[d] *ISTERRE, CNRS et Université Joseph Fourier, Grenoble, France*

Abstract

Observations of both fast and slow propagating ruptures on earthquake faults suggest a close relation between the two phenomena. Earthquakes are the signature of fast ruptures on localized asperities while slow aseismic deformations are experienced on other parts of the fault plane. However, the mechanism linking earthquakes and the aseismic processes is still unclear due to the difficulty of imaging these phenomena of large spatiotemporal variability at depth. Here, we present laboratory experiments that explore deformation processes of heterogeneous media in the brittle-creep regime. We track the evolution of an interfacial crack over 7 orders of magnitude in time and 5 orders of magnitude in space using an optical camera and acoustic sensors. We explore the response of the system to slow transient loads and show that slow deformation episodes are systematically accompanied by acoustic emissions. At small scales, these acoustic emission events are closely

*Corresponding author
Email address: lengline@unistra.fr (O. Lengliné)

related to the activity of local creep. Similar statistical features of both the acoustic emission activity and the deformation rate distribution between our system and faults suggest an active role of local creep deformation in driving the seismic activity of earthquake swarms.
Keywords:

---

1. Introduction

Numerous observations of a correlation between the enhancement of the seismic activity and the simultaneous detection of slow slip transients in the Earth crust have been reported in recent years. Such concurrent increase of seismicity and deformation rate has been observed in various tectonic locations (Linde et al., 1996; Crescentini et al., 1999; Lohman and McGuire, 2007; Segall et al., 2006; Liu et al., 2007) as well as in geothermal areas (Bourouis and Bernard, 2007; Takada and Furuya, 2010). Also, observations of postseismic slip following large earthquakes are manifestations of transient deformation coupled with abundant earthquake activity, i.e. aftershocks (Perfettini and Avouac, 2004).

In some cases, the seismic signal concurrent with slow slip events is characterized as tectonic tremors or low frequency earthquakes as observed in subduction zones (Rogers and Dragert, 2003; Obara et al., 2004; Ito et al., 2007) or in transform tectonic settings like the San Andreas Fault (SAF) (Vidale and Shearer, 2006; Nadeau and Dolenc, 2005; Shelly, 2010). Also the aseismic nucleation phase of mainshocks have been related to foreshocks such as in the case of the 1999 Izmit earthquake (Bouchon et al., 2011) or the 2011 Tohoku-Oki earthquake (Miyazaki et al., 2011; Ando and Imanishi,

2011)

Seismic events associated with aseismic slips are generally located on fault planes suggesting that they represent a dynamic shear instability on the sliding interface (La Rocca et al., 2009; Shelly et al., 2009). Geodetic inversions pinpoint the aseismic motion to be occurring on the same fault plane structure (Lohman and McGuire, 2007). However the deformation signal recorded at the surface by GPS and/or InSAR instrument only provides a macroscopic view of the deformation process at depth. Details of the aseismic slip distribution are often lacking due to the limited resolution. In some cases, when aseismic slip exists at the surface, slip distribution is accessible from InSAR survey (Doubre and Peltzer, 2007).

The close spatial and temporal occurrence of both seismic and aseismic slip suggests a causal relation between the two phenomena. Nonetheless, the causal mechanism is not straightforward as earthquakes can both trigger and be triggered by slow slip events (Du et al., 2003; Perfettini and Avouac, 2004). It might also be that both aseismic and seismic slips are manifestations of a common deformation process. In this case, the seismic signal can be seen as the signature of patches of the fault plane deforming dynamically whereas the geodetic observation represents an integrated signal over all the deforming sites. Therefore, the deformation on a fault plane takes place over a wide range of speeds. This is supported by observations of heterogeneous postseismic slip on the SAF inferred from the analysis of repeating earthquake sequences (Lengliné and Marsan, 2009). The dynamic events represent the high velocity tail of the slip speed distribution while its average produces the observed geodetic signal.

The contribution of earthquakes to the total amount of slip released during transient episodes is generally small (Lohman and McGuire, 2007). Despite being located on a common interface, the precise spatial location of the seismic activity relative to the aseismic slip is difficult to obtain with a high resolution. The interface property might control the partition between seismic and aseismic slip, the interface being envisioned as a zone with strong patches (asperities) embedded in an otherwise low resistance region which accommodates slow slip (Linde et al., 1996; Lohman and McGuire, 2007; Wech et al., 2009; Perfettini et al., 2010). The concentration of asperities, or brittle patches, governs the relative importance of dynamic failures in the deformation process. It is also readily possible that temperature produces a broad scale effect on the slip partition over the interface and thus constrains the transition between brittle and ductile rheology.

The physics of crustal mechanics of both seismic and aseismic processes is not straightforward as it involves a complex problem of a spatially heterogeneous medium with a large number of degrees of freedom and short and long range interactions. Several numerical models have tried to reproduce the evolution of such systems but computations are very time consuming and limited to only large scale heterogeneities (Kaneko et al., 2010), or to the quasi-dynamics appropximation (Hillers et al., 2007; Ariyoshi et al., 2011). Experimental configurations overcome these difficulties as space-time integrations are performed by the deforming system without any model requirement. Here, we investigate the slow (creep) and fast (acoustic) deformations produced by the propagation of an interfacial brittle-creep crack. Our experimental setup is a much simpler configuration than that of a complex

fault zone system but the fundamental processes of interest, the slow deformation and brittle fracture in heterogeneous media, remain similar. Our setup allows the monitoring, at the same time, of both acoustic activity and the detailed geometrical evolution of the fracture. We show that seismic and aseismic events co-exist in the system. Acoustic and creep event rates are highly correlated with a significant increase of the slow event activity simultaneously with the rise of acoustic event activity. It suggests that seismic activity during swarm episodes is driven by the elastic loading of local aseismic deformations on strong asperities.

2. Experimental Setup

2.1. Sample Preparation

To prepare each sample, we use two transparent PMMA plates of dimensions $20 \times 10 \times 1.0\, cm$ and $23 \times 2.8 \times 0.5\, cm$ (Figure 1). First, we sand-blast one surface of the narrow plate with glass beads of diameter $\phi \in [180 - 300]\, \mu m$. We clean the blasted plate to remove any electrically attached glass beads. Then we assemble the two plates in a stiff metallic loading cell with the blasted surface facing a surface of the larger plate. Finally, we impose an homogeneous normal load on the assembled plates and heat the loaded sample at $190°C$ for 45 minutes to anneal the plates. The thermal annealing produces a weak cohesive interface along which the sample will breaks under load. The sand-blasting introduces a random roughness of the plate surface that controls the local strength along the weak interface. It also induces microstructures at the plate surface which make the sample opaque, but the newly formed block, after annealing, recovers its transparency since the con-

trast of the refraction index along the interface disappears (see Grob et al. (2009); Lengliné et al. (2011) for details). Interestingly PMMA exhibits a brittle behavior at short time scales and is semi-brittle or even plastic at longer times. Macroscopically this long time scale regime is described by a ductile rheology. PMMA shows a time-temperature equivalence desirable for addressing either high temperature processes or very long term evolution (Ward and Hadley, 1993). This richness of the PMMA rheology enables the observation of a brittle-creep rupture regime. It provides an attractive analogy for the study of numerous time-dependent mechanisms in the Earth's crust as those originating at the brittle-ductile transition.

2.2. Mechanical loading

Once the sample is ready, we clamp the widest PMMA plate to a stiff aluminum frame. A stepping motor applies the loading over the top side of the narrow plate in a direction normal to the plate interface (Figure 1). We measure the vertical displacement of the loading point with a linear variable differential transformer (LVDT) with a resolution of $1.3\,\mu m$. The vertical displacement imposed on the narrower plate induces stable mode I propagation of a planar fracture along the prescribed weak interface. We impose a variation of the loading speed, $\dot{u}(t)$, to simulate a variation of the external driving force. We introduced various forms of transients: step increase, bump and sine changes of the loading speed which all produce broad scale variation of the front speed (e.g. Figure 2). These external loading fluctuations could be interpreted as an analog for far field stress perturbations caused by example by pore fluid pressure, magmatic intrusion or mantle flow.

2.3. Optical events

We monitor the fracture front propagation using a fast optical camera (CamRecord 600) with up to 1000 fps or a slow speed camera (Nikon D700) with up to 5 fps to follow the progression of the average front position over longer time scales (Figure 1). Optical images of the interfacial rupture show dark and bright regions respectively corresponding to open crack and unbroken parts of the sample. Image processing determines the transition between dark and bright areas that defines the fracture front. We first compute the difference between each image and the first image of the experiment. The image difference highlights the fracture front while removing permanent artifacts. Then, grayscale images are transformed into black and white images according to a gray level threshold separating bright and dark regions. Then, we calculate the gradient in the direction of front propagation to highlight the transition zone. We finally extract connected pixels from the gradient images that correspond to the front position, $a(x,t)$. The front propagates along the y axis with the origin defined at the load point and is positive in the direction of crack propagation. The x axis is perpendicular to y and defines the coordinate of a point along the front and $\bar{a}(t)$ is the mean position of the front at time t (see Måløy et al. (2006) and Grob et al. (2009) for details). We compute the local speed of the crack by integrating the time spent by the front line in each pixel and then take its inverse (Figure 3). We extract from the local movements of the front, those with the highest speed. Similarly to the broad scale variation of the front velocity which could be compared to slow event recorded by geodetic instruments in a tectonic context, such patches of local higher than average deformation speed could be considered

as analogous to local creeping episode or slow slip events. They represent slow deformation episodes that locally exceeds the macroscopic deformation rate. In order to define such events, we follow the procedure detailed by Grob et al. (2009). We fix a speed threshold, v_{th} defining the required speed to define an optical event. Here we use $v_{th} = 10 \times \langle v \rangle$, where $\langle v \rangle$ is the mean velocity of the crack during an experiment. An optical event is identified as a cluster of connected pixels satisfying the velocity threshold condition. Although these optical events have higher velocities than most of the deforming sites, they remain slow deformation episodes compared to dynamic events (since the average speed is around $\langle v \rangle \simeq 500 \mu m s^{-1}$, far from the Rayleigh wave speed, $V_r \simeq 1.710^9 \mu m s^{-1}$). These optical events are characterized by a Gutenberg-Richter law with the power law slope being similar to that for tectonic earthquakes (Grob et al., 2009). This Gutenberg-Richter relation might also be linked to the magnitude-frequency scaling inferred for slow-slip events (Wech et al., 2010).

2.4. Acoustic events

The crack propagation produces acoustic activity that we monitor with a 32 elements linear array of piezo-electric sensors. Sensors are located on a line parallel to the plate axis and sensor centers are spaced by 3 mm. The typical distance between the closest acoustic sensor and the border of the plate is 1 cm. The sensors peak frequency response is $\sim$ 500 kHz and continuous recording on all channels is at 5 MHz. For each experiment, we extract the acoustic signal recorded in the two closest acoustic sensors to the crack front line. We manually trigger the acquisition of the acoustic and it is synchronized with the camera time. The recording of the acoustic signal

lasts, in our experiments, for a maximum of 50 s.

We use a short-term-average to long-term-average ratio (STA/LTA) to detect acoustic events (AE) in the recorded acoustic signal (Earle and Shearer, 1994). This procedure is similar to the one applied to earthquake data but we use shorter time windows to deal with our short signal durations. The STA window length is $20\mu s$, the LTA window length is $100\mu s$ and the threshold for setting an STA/LTA detection is 2.0. An event must be detected simultaneously on the two closest channels to be considered in our analysis. We show an example of the acoustic signal recorded during one experiment in figure 4. The typical duration of the recorded events is on the order of $100\mu s$. The performance of the detection algorithm is illustrated in figure 5. As expected, event detection is associated with high amplitudes of the recorded signal on the two closest channels. We observe non-uniformly distributed clustering of acoustic activity along with the optical events (figure 5). The temporal coincidence between AEs and OEs is not perfect (figure 5). This can be attributed to AEs that are too small to be optically detected, OEs that are genuinely aseismic, and clusters of AEs that are lumped into a single large OE.

3. Results

3.1. Distribution of inter-event time

Our results, shown in figure 5, suggest the presence of clustering of the acoustic activity. We quantify the clustering by calculating the distribution of inter-event times of successive AE for all experiments. Temporal clustering has been well documented for earthquakes and is suggested to be a result

of interactions among earthquake sites (Corral, 2004; Molchan, 2005; Hainzl et al., 2006; Saichev and Sornette, 2007). We compute inter-event time between successive AE for all the 14 experiments. For each experiment we only considered AE when the loading rate was nearly constant in order to avoid mixing populations recorded during different loading rates. Inter-event times are normalized by the average AE rate of each experiment (the average AE rate for the different experiments, is of the order of 10^2 events/sec). Therefore, the probability density functions (pdf) obtained from all experiments can be represented on the same plot and well approximated by a gamma function (Fig 6) proposed for earthquakes (Corral, 2004). The gamma distribution in figure 6 is obtained from the averaging of the parameters of each individual fit. Fig. 6 also includes the inter-event time distribution for the ISC worldwide catalog for earthquakes with magnitude M>5.5 in the period 1975-2004. The normalization of the interevent time is obtained similarly by the average seismic event rate (of the order of 1 event/day). The good agreement of the gamma distribution with the pdf obtained from our experimental data, is similar to the agreement obtained for earthquake data (Corral, 2004) or AE recorded during rock fracture experiments (Davidsen et al., 2007). It suggests that the mechanism responsible for the seismic activity in fault systems or rock fractures, share strong similarities with our experiments. The decay at short time scale is interpreted as the emergence of an Omori-Utsu law describing interactions among the events while at longer time scales the distribution evolves to an exponential distribution representative of a Poisson process (Saichev and Sornette, 2007).

3.2. Power-law distribution of local slip-rate

We calculate the pdf of the local velocities following Måløy et al. (2006) for 6 of the experiments where we used the fast video camera at high sampling rate. We only analyze, for these experiments, time windows with an almost constant large scale velocity. The local velocity is normalized by the average velocity of the crack, $\langle v \rangle$. Front velocities exhibit significant fluctuations at small scales (Figure 3). For $v > \langle v \rangle$ the pdf shows a power law decay with exponent 2.55 consistent with previous work (Måløy et al., 2006; Lengliné et al., 2011). This power law behavior of the deformation rate at small scale in our experiment is similarly observed in natural fault systems. In southern California, fault slip rates are found to obey a power law scaling with most of the fault system characterized by slow slip rates (Meade, 2007). It suggests that this scaling behavior is a general feature of slowly deforming medium in the presence of heterogeneities.

3.3. Comparison of AE and OE activity

We simultaneously monitor the evolution of the AE rate with the spatial average velocity of the crack front and the optical event (OE) rate in a time segment encompassing the loading transient (Figure 2). We show the evolution of the AE and OE rates and the average crack front speed during a transient episode (Figure 7). AE, OE rates and average front velocity are computed for intervals of 0.2 s. We notice that at the order of a few seconds, rate of acoustic emission, average front speed and OE rate exhibit a very similar evolution. A clear temporal relation between these three quantities at this large scale can be inferred: the AE and OE rates closely follow the macroscopic variation of crack front speed.

In order to quantify the relationship between the average crack front velocity and the AE rate, we compute the affine relation linking these two quantities for all experiments. The residuals of the linear relation are small and symmetrically distributed suggesting that a linear form might represent a reasonable relation between AE rate and crack velocity. This is attested by the correlation coefficient, ρ, computed for each experiments between these two variables. The correlation coefficient is defined as $\rho = \sigma_{xy}/\sigma_x\sigma_y$, with σ_{xy} the covariance of the AE rate with the front speed and σ_x and σ_y the standard deviations of the AE rate and the front speed. The correlation coefficient, ρ for window size of 0.2 s and for our 14 experiments ranges from $\rho = 0.75$ to 0.97 and with a mean value of 0.87.

3.4. An interplay of seismic and aseismic local deformations

We now focus to smaller time scales in order to decipher the link between acoustic activity and slow movement of the crack front. The crack front velocity shows some fluctuations at small scales, although smooth and rather continuous when observed at large scale. These fluctuations result from the heterogeneous nature of the interface and elastic interactions along the crack front line. We investigate the temporal relation between optical and acoustic events recorded during the 6 experiments that show the highest acoustic activity and the best resolved crack propagation. We show in Figure 8 the cross-correlation function, $C(\Delta t)$, between the rate of AE, $r_{AE}(t)$, and the rate of optical events, $r_{OE}(t)$. For both AE and optical events, rate are computed as the number of events detected in time interval of 5 ms from time t_0 to time t_f, and mean is remove from the time-series. The cross-

correlation function is obtained as

$$C(\Delta t) = \frac{1}{\sqrt{C_{AE} C_{OE}}} \sum_{t_0}^{t_f} r_{OE}(t + \Delta t) \times r_{AE}(t), \quad (1)$$

where C_{AE} and C_{OE} are the auto-correlations values of the AE and the OE rates respectively at zero lag time. We observe that the maximum correlation between the two types of signal is obtained at zero lag time. It suggests that the acoustic activity occurs mostly in a short time span around the aseismic deformation. The almost symmetric shape of the correlation function also suggests that optical events both precede and follow acoustic activity during the course of an experiment highlighting the close interplay between these two modes of deformation. The slight asymmetrical shape of $C(\Delta t)$ observed in Figure 8 also suggests that a higher rate of OE occurs following AE than preceding it, similar to postseismic slip observed after earthquake.

4. Conclusion

We analyze the coupled evolution of acoustic activity and slow deformation during the propagation of a brittle-creep fracture in an heterogeneous medium. Our unique experimental setup allows to address the link that takes place between seismic and aseismic slip along natural fault. It provides an original characterization of slow deformation processes that are difficult to capture on faults at depth. Numerous statistical features of the deformation observed in natural systems are reproduced by our experiment like gamma distribution of interevent time or power law distribution of slip rate. We show that the acoustic activity (dynamic events) is part of the deformation process which occurs over a widely distributed range of speeds including

slow slip. Indeed, small scale observation of the deformation reveals links between creep and acoustic events. The small scale complex dynamics leads to a macroscopic integrated signal of the deformation which shows a smooth and continuous deformation speed and which correlates well with the rate of acoustic events.

Acknowledgments

We thank K. J. Måløy, K. T. Tallakstad, S. Santucci, M. Grob, F. H. Cornet, J.P. Avouac, D. R. Shelly, M. Aktar and H. Karabulut for fruitful discussions. We acknowledge the support of ANR grant SUPNAF and of NSF grant EAR-1015698.

References

Ando, R., Imanishi, K., 2011. Possibility of Mw 9.0 mainshock triggered by diffusional propagation of after-slip from mw 7.3 foreshock. Earth, Planets and Space 63, 767–771.

Ariyoshi, K., Matsuzawa, T., Ampuero, J.-P., Nakata, R., Hori, T., Kaneda, Y., Hino, R., Hasegawa, A., 2011. Migration process of very low-frequency events based on a chain-reaction model and its application to the detection of preseismic slip for megathrust earthquakes. Earth, Planets and Space, in press.

Bouchon, M., Karabulut, H., Aktar, M., Özalaybey, S., Schmittbuhl, J., Bouin, M.-P., 2011. Extended Nucleation of the 1999 M_w 7.6 Izmit Earthquake. Science 331, 877.

Bourouis, S., Bernard, P., 2007. Evidence for coupled seismic and aseismic fault slip during water injection in the geothermal site of Soultz (France), and implications for seismogenic transients. Geophys. J. Int. 169, 723–732.

Corral, A., 2004. Long-term clustering, scaling, and universality in the temporal occurrence of earthquakes. Phys. Rev. Lett. 92, 108501.

Crescentini, L., Amoruso, A., Scarpa, R., 1999. Constraints on slow earthquake dynamics from a swarm in central Italy. Science 286 (5447), 2132–2134.

Davidsen, J., Stanchits, S., Dresen, G., 2007. Scaling and universality in rock fracture. Phys. Rev. Lett. 98, 125502.

Doubre, C., Peltzer, G., 2007. Fluid-controlled faulting process in the asal rift, djibouti, from 8 yr of radar interferometry observations. Geology 35 (1), 69–72.

Du, W.-x., Sykes, L. R., Shaw, B. E., Scholz, C. H., 2003. Triggered aseismic fault slip from nearby earthquakes, static or dynamic effect? J. Geophys. Res. 108, 2131.

Earle, P. S., Shearer, P. M., 1994. Characterization of global seismograms using an automatic-picking algorithm. Bull. Seis. Soc. Am. 84 (2), 366–376.

Grob, M., Schmittbuhl, J., Toussaint, R., Rivera, L., Santucci, S., Måløy, K. J., 2009. Quake catalogs from an optical monitoring of an interfacial crack propagation. Pure App. Geophys. 166, 777–799.

Hainzl, S., Scherbaum, F., Beauval, C., 2006. Estimating Background Activity Based on Interevent-Time Distribution. Bull. Seism. Soc. Am. 96, 313–320.

Hillers, G., Mai, P. M., Ben-Zion, Y., Ampuero, J.-P., 2007. Statistical properties of seismicity of fault zones at different evolutionary stages (in press). Geophys. J. Int. 169, 515–533.

Ito, Y., Obara, K., Shiomi, K., Sekine, S., Hirose, H., 2007. Slow Earthquakes Coincident with Episodic Tremors and Slow Slip Events. Science 315, 503–.

Kaneko, Y., Avouac, J.-P., Lapusta, N., 2010. Towards inferring earthquake patterns from geodetic observations of interseismic coupling. Nature Geoscience 3, 363–369.

La Rocca, M., Creager, K. C., Galluzzo, D., Malone, S., Vidale, J. E., Sweet, J. R., Wech, A. G., 2009. Cascadia Tremor Located Near Plate Interface Constrained by S Minus P Wave Times. Science 323, 620–.

Lengliné, O., Marsan, D., 2009. Inferring the coseismic and postseismic stress changes caused by the 2004 $M_w = 6$ Parkfield earthquake from variations of recurrence times of microearthquakes. J. Geophys. Res. 114, B10303.

Lengliné, O., Schmittbuhl, J., Elkhoury, J., Ampuero, J. P., Toussaint, R., Måløy, K. J., 2011. Down-scaling of fracture energy during brittle creep experiments. J. Geophys. Res. 116.

Linde, A. T., Gladwin, M. T., Johnston, M. J. S., Gwyther, R. L., Bilham, R. G., Sep. 1996. A slow earthquake sequence on the San Andreas fault. Nature 383, 65–68.

355 Liu, Y., Rice, J. R., Larson, K. M., 2007. Seismicity variations associated
356 with aseismic transients in Guerrero, Mexico, 1995 2006. Earth Planet.
357 Sci. Lett. 262, 493–504.

358 Lohman, R. B., McGuire, J. J., 2007. Earthquake swarms driven by aseismic
359 creep in the Salton Trough, California. J. Geophys. Res. 112, B04405.

360 Måløy, K. J., Santucci, S., Schmittbuhl, J., Toussaint, R., 2006. Local waiting
361 time fluctuations along a randomly pinned crack front. Phys. Rev. Lett.
362 96, 045501.

363 Meade, B. J., 2007. Power-law distribution of fault slip-rates in southern
364 California. Geophys. Res. Lett. 342, L23307.

365 Miyazaki, S., McGuire, J. J., Segall, P., 2011. Seismic and aseismic fault slip
366 before and during the 2011 off the Pacific coast of Tohoku earthquake.
367 Earth, Planets and Space 63, 637–642.

368 Molchan, G., 2005. Interevent Time Distribution in Seismicity: A Theoretical
369 Approach. Pure Appl. Geophys. 162, 1135–1150.

370 Nadeau, R. M., Dolenc, D., 2005. Nonvolcanic tremors deep beneath the san
371 andreas fault. Science 307 (5708), 389.

372 Obara, K., Hirose, H., Yamamizu, F., Kasahara, K., 2004. Episodic slow slip
373 events accompanied by non-volcanic tremors in southwest Japan subduc-
374 tion zone. Geophys. Res. Lett. 31, L23602.

375 Perfettini, H., Avouac, J.-P., 2004. Postseismic relaxation driven by brittle
376 creep: A possible mechanism to reconcile geodetic measurements and the

decay rate of aftershocks, application to the Chi-Chi earthquake, Taiwan. J. Geophys. Res. 109, B02304.

Perfettini, H., Avouac, J.-P., Tavera, H., Kositsky, A., Nocquet, J.-M., Bondoux, F., Chlieh, M., Sladen, A., Audin, L., Farber, D. L., Soler, P., 2010. Seismic and aseismic slip on the Central Peru megathrust. Nature 465, 78–81.

Rogers, G., Dragert, H., 2003. Episodic Tremor and Slip on the Cascadia Subduction Zone: The Chatter of Silent Slip. Science 300, 1942–1943.

Saichev, A., Sornette, D., 2007. Theory of earthquake recurrence times. J. Geophys. Res. 112, B04313.

Segall, P., Desmarais, E. K., Shelly, D., Miklius, A., Cervelli, P., 2006. Earthquakes triggered by silent slip events on Kīlauea volcano, Hawaii. Nature 442, 71–74.

Shelly, D. R., 2010. Migrating tremors illuminate complex deformation beneath the seismogenic San Andreas fault. Nature 463, 648–652.

Shelly, D. R., Ellsworth, W. L., Ryberg, T., Haberland, C., Fuis, G. S., Murphy, J., Nadeau, R. M., Bürgmann, R., 2009. Precise location of San Andreas Fault tremors near Cholame, California using seismometer clusters: Slip on the deep extension of the fault? Geophys. Res. Lett. 36, L01303.

Takada, Y., Furuya, M., 2010. Aseismic slip during the 1996 earthquake swarm in and around the Onikobe geothermal area, NE Japan. Earth Planet. Sci. Lett. 290, 302–310.

400 Vidale, J. E., Shearer, P. M., May 2006. A survey of 71 earthquake bursts
401 across southern California: Exploring the role of pore fluid pressure fluc-
402 tuations and aseismic slip as drivers. J. Geophys. Res. 111, B05312.

403 Ward, I. M., Hadley, D. W., 1993. An introduction to the mechanical prop-
404 erties of solid polymers. Wiley.

405 Wech, A. G., Creager, K. C., Houston, H., Vidale, J. E., Nov. 2010. An
406 earthquake-like magnitude-frequency distribution of slow slip in northern
407 Cascadia. Geophys. Res. Lett. 372, L22310.

408 Wech, A. G., Creager, K. C., Melbourne, T. I., 2009. Seismic and geodetic
409 constraints on Cascadia slow slip. J. Geophys. Res. 114, B10316.

Figure 1: Side view (left) and bottom view (right) of the experimental setup. A stiff aluminum frame is attached to the upper PMMA plate. The bottom plate is separated from the upper one using a loading force applied by a rod connected to a stepping motor. The load causes a deflection u of the bottom plate and the propagation of an interfacial crack. The crack front is located at distance $\bar{a}$ from the free end. The front advance is monitored by a high or slow speed camera set in vertical position, perpendicular to the crack plane.

Figure 2: Evolution of the force (red), and loading point displacement (blue) during an experiment. The crack is supposed to start moving around $t = 45s$ as evidenced by the peak of force. The black box on the top figure represents a zoom displayed on the bottom figure. We see that the loading point position is imposed a transient variation of speed between t = 65 s to 85 s with the aim of simulating a transient variation of speed of the crack front (the black line corresponds to the front position). The camera and acoustic time window are displayed as dark gray and light gray shaded area.

Figure 3: **A**: Map of the local speeds of the front on the interface. Dimension of the interface can be appreciated from the length of the vector showing the front propagation direction which is 1.3 mm long. The front propagates from bottom to top. We observe small scale fluctuations of the crack front speed. Black dots represent optical events obtained after thresholding the velocity map and are displayed at the centroid of the corresponding high velocity cluster. **B**: Zoom on an inset portion of the interface represented by the black rectangle in **A**. **C**: Probability density functions (pdfs) of the local velocities computed for 6 experiments. We observe a power law decay of the pdfs for $v > \langle v \rangle$ with an exponent $\nu = -2.55$ compatible with Måløy et al. (2006).

Figure 4: Example of recorded signal for an acoustic event. We observed a modification of the frequency content associated with the arrival of the AE wave train. The duration of the AE on the displayed channel is around $100\mu s$.

Figure 5: Acoustic records on two channels for 100 ms during one experiment. We observe on these two channels an abundant activity as attested by the numerous peaks in the acoustic signals. Stars mark the identification of events after processing of the two signals by the STA/LTA procedure and matching common detection. The histogram in red indicates the optical events recorded during the same time period.

Figure 6: Distribution of normalized inter-event time for all experiments. Each experiment is represented by a different colour. The best gamma distribution fitting all the experiments is represented by a black curve and is $p(\tau) = C\tau^{\gamma-1}e^{-\tau/\beta}$, where $C = 0.44$, $\beta = 1.8$ and $\gamma = 0.54$. Black filled diamonds show the inter-event time distribution computed from the ISC worldwide catalog for earthquakes with magnitude M > 5.5.

Figure 7: Evolution of the rate of AE (purple diamonds), of the average crack front speed (blue squares) and of the optical event (OE) rate (red circles) as a function of time. Rate are computed for interval of 0.2 s. We observe that the rate of AE and OE is well correlated with the variation of the crack front speed at this broad scale.

Figure 8: Cross-correlation function $C(\Delta t)$ between the rate of acoustic events and the rate of optical events. AE rate and OE rate are computed as the number of events for intervals of 5 ms and mean is remove from the time-series. The cross-correlation function corresponds to an averaged function computed over 6 experiments. We observe that the maximum of the correlation function is found at zero time lag. We also notice the increase of the correlation function around the peak, suggesting that OE are clustered in time for some duration before and after an AE. The inset figure shows the normalized autocorrelation functions for the AE (black curve) and the OE (gray curve). Both functions show some increase around zero time lag supporting the interplay between these two modes of deformation.

***Highlights**

> We build an original experiment designated to study the relation between slow and dynamic deformations in the brittle creep regime.
> We observe numerous acoustic events in relations with local creeping episodes.
> In relation with faulting processes, we propose that earthquake swarms are driven by local slow slips.

Figure 1a

Click here to download Figure: fig1a.eps

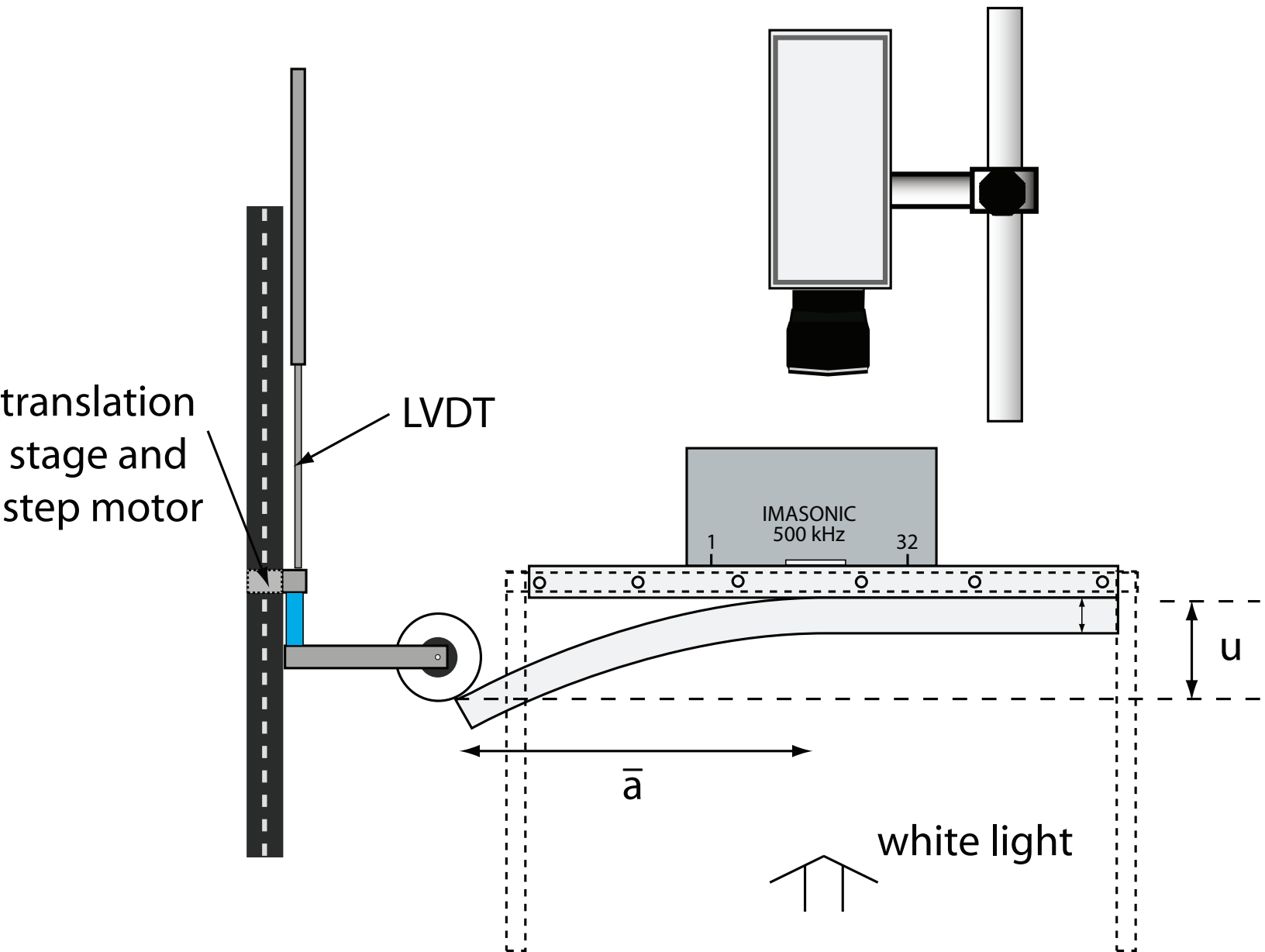

Figure 1b

Click here to download Figure: fig1b.eps

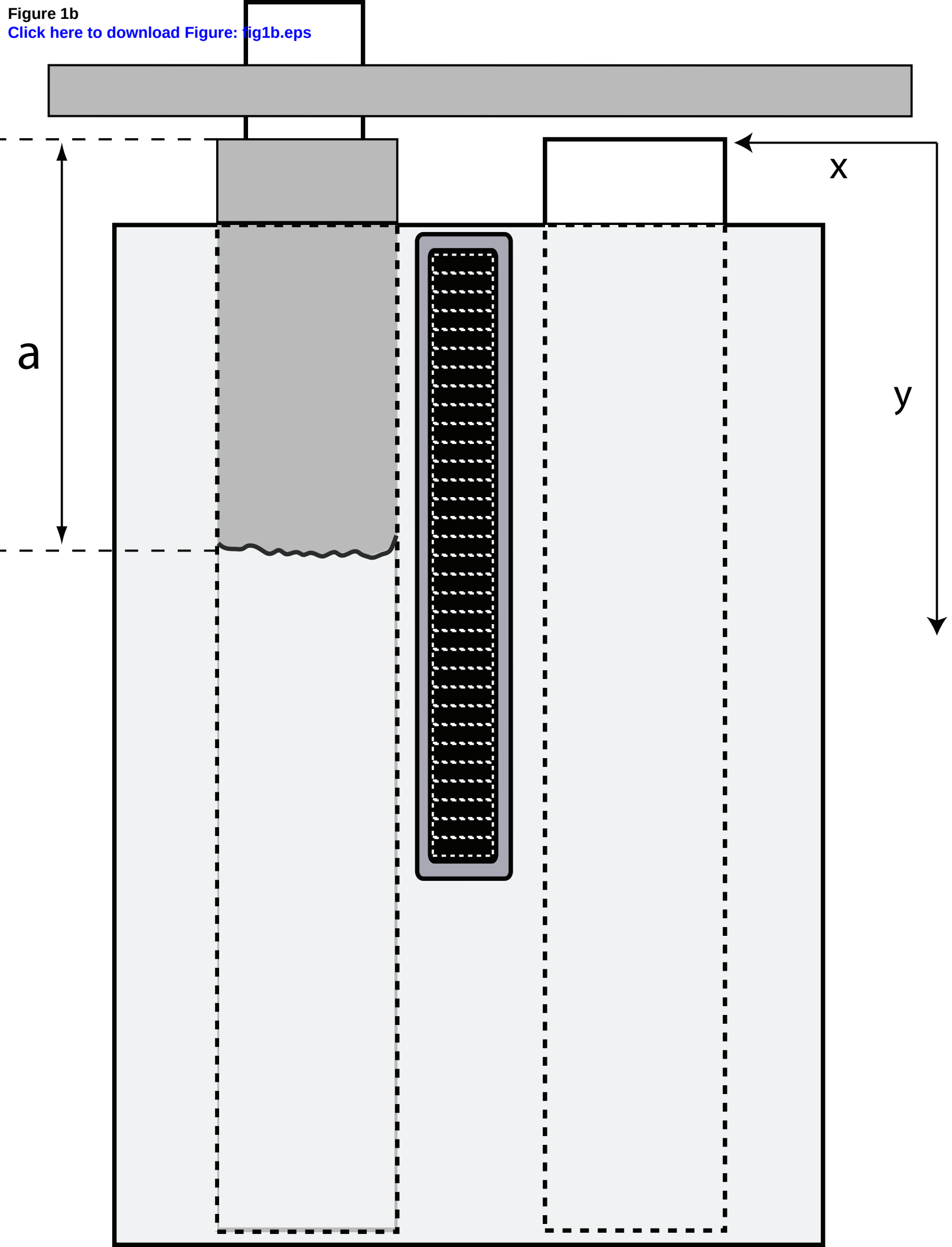

Figure 2

Click here to download Figure: fig2.eps

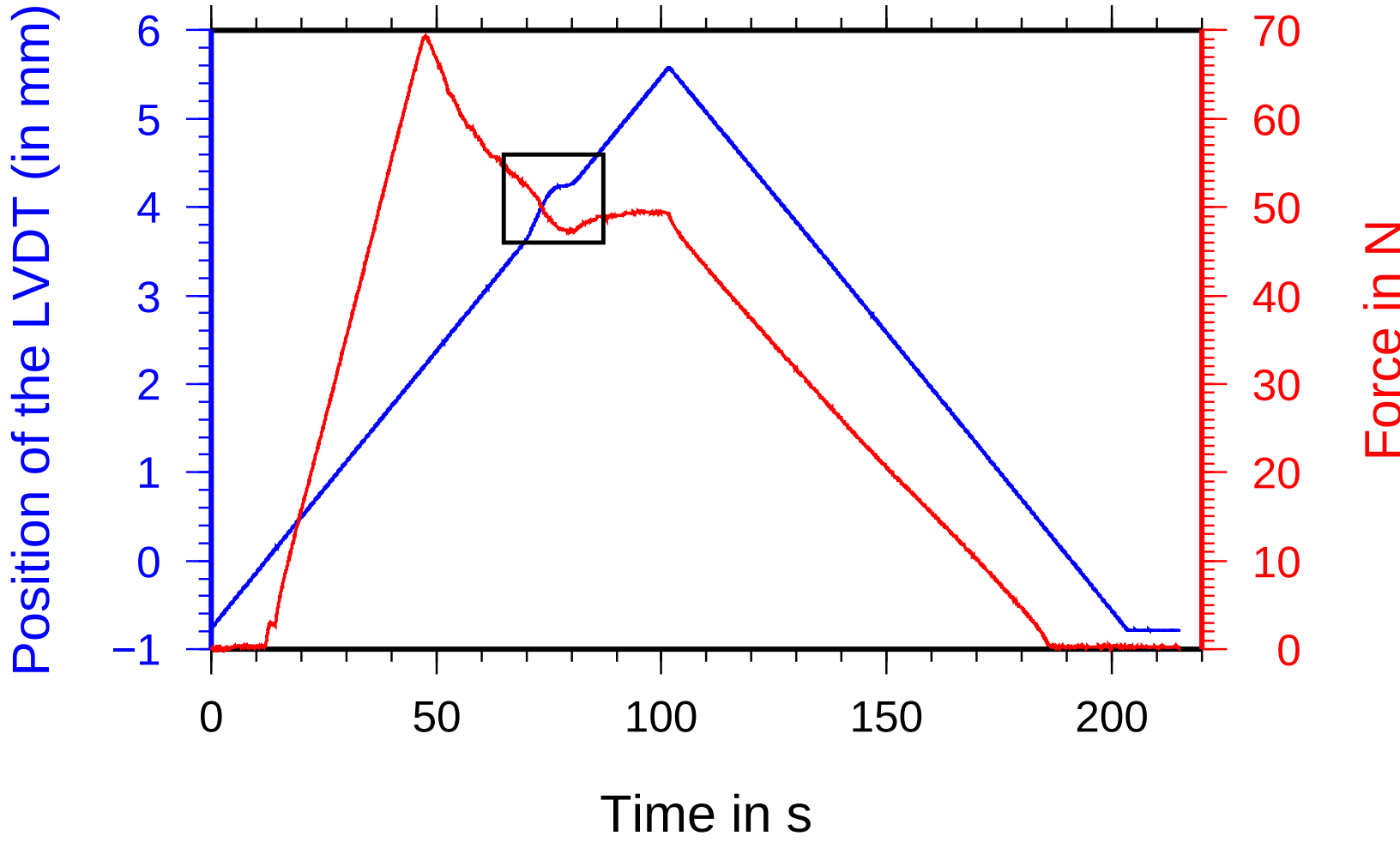

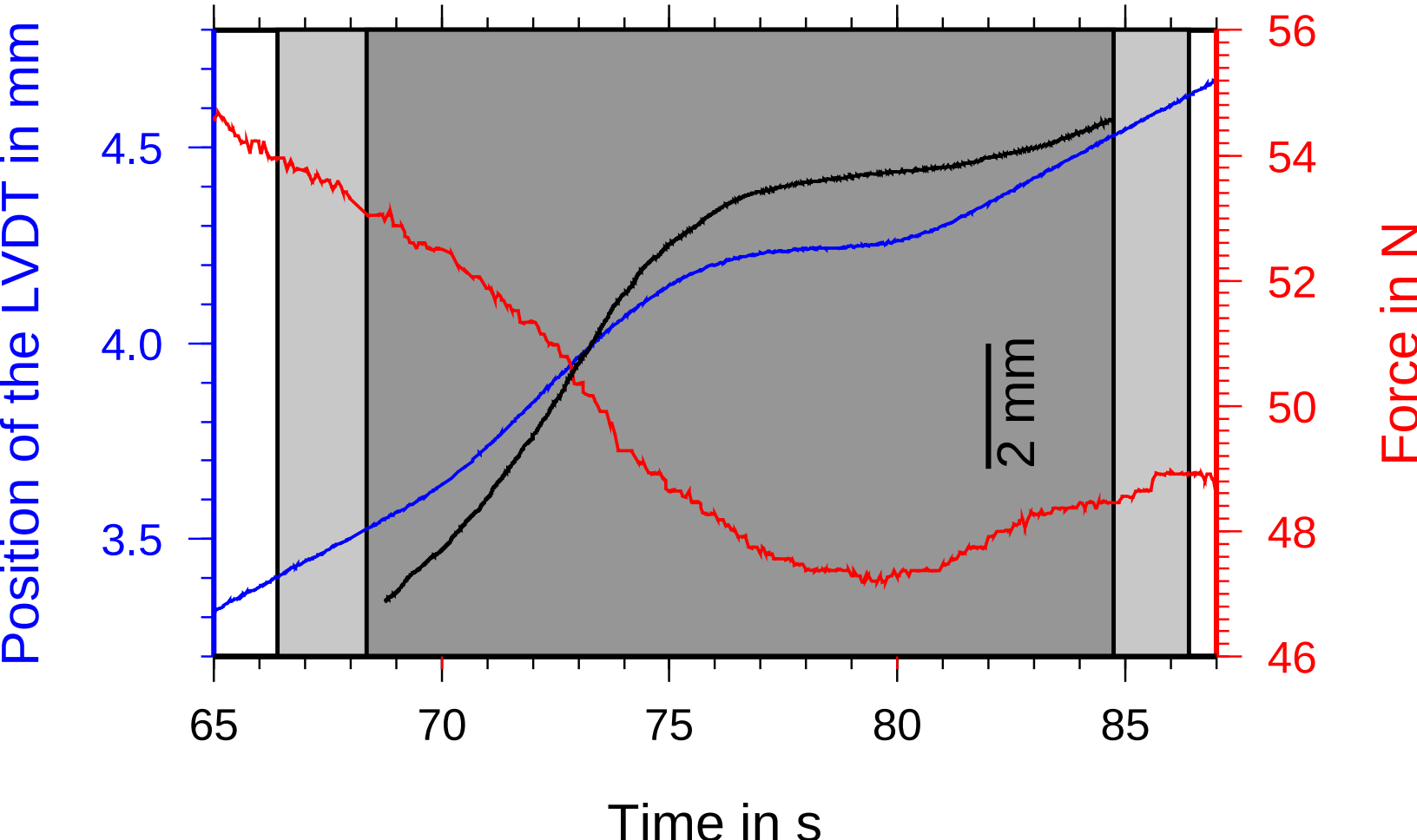

Figure 3
Click here to download Figure: fig3.eps

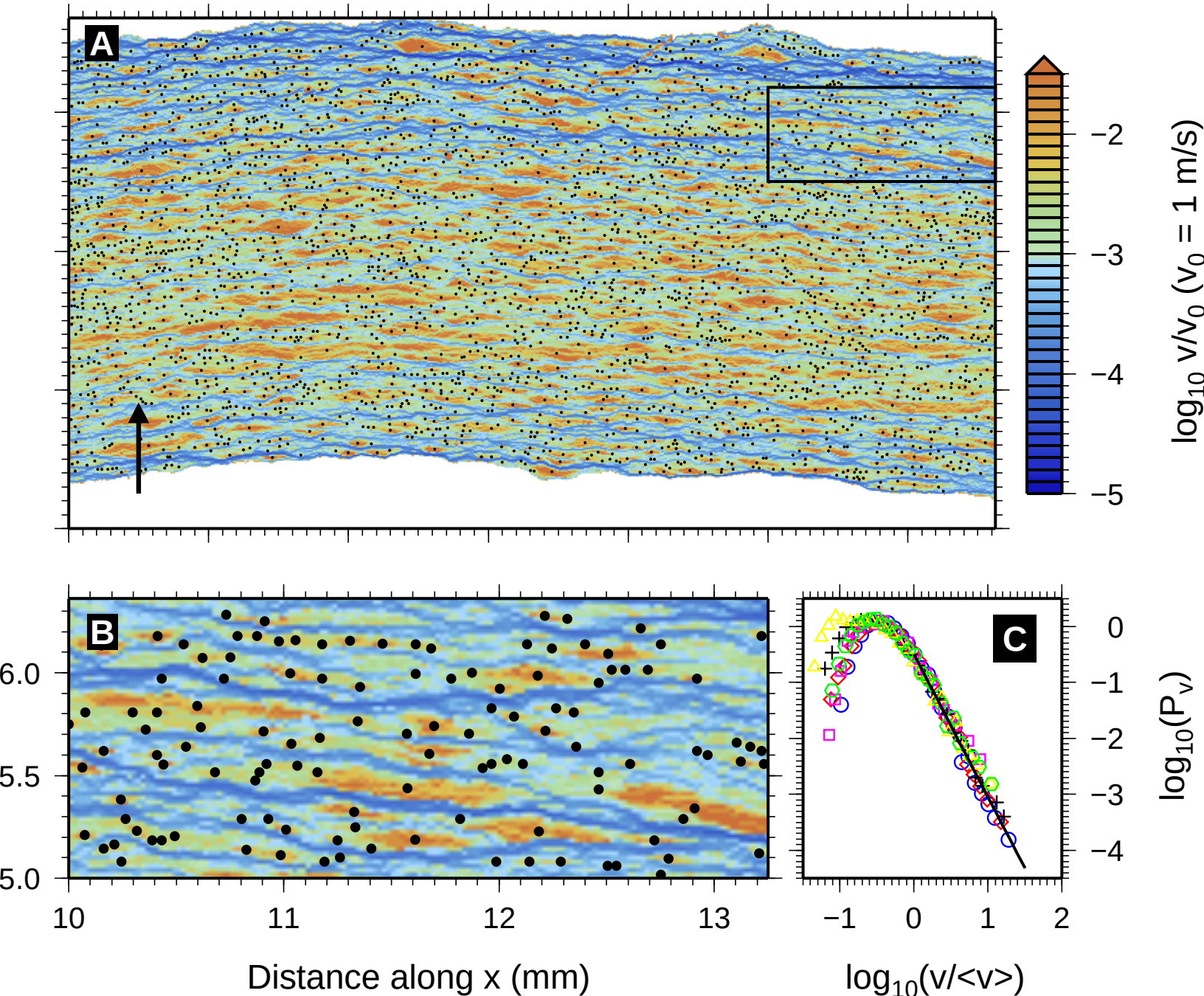

Figure 4
Click here to download Figure: fig4.eps

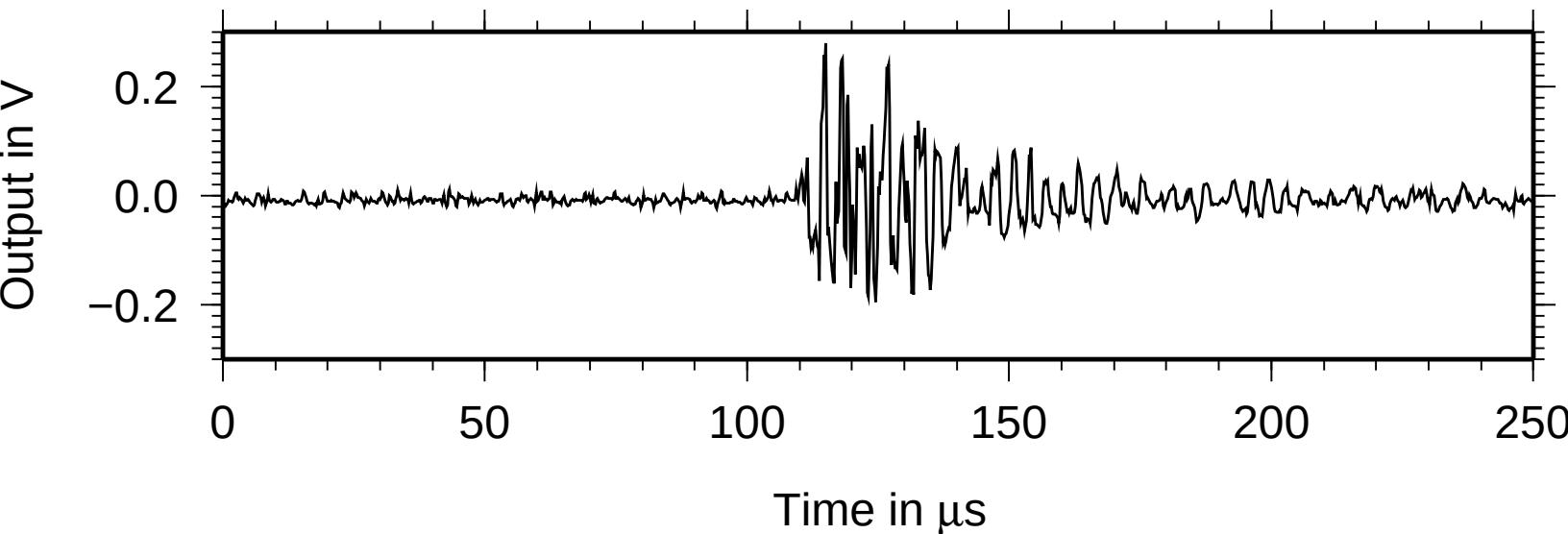

Figure 5

Click here to download Figure: fig5.eps

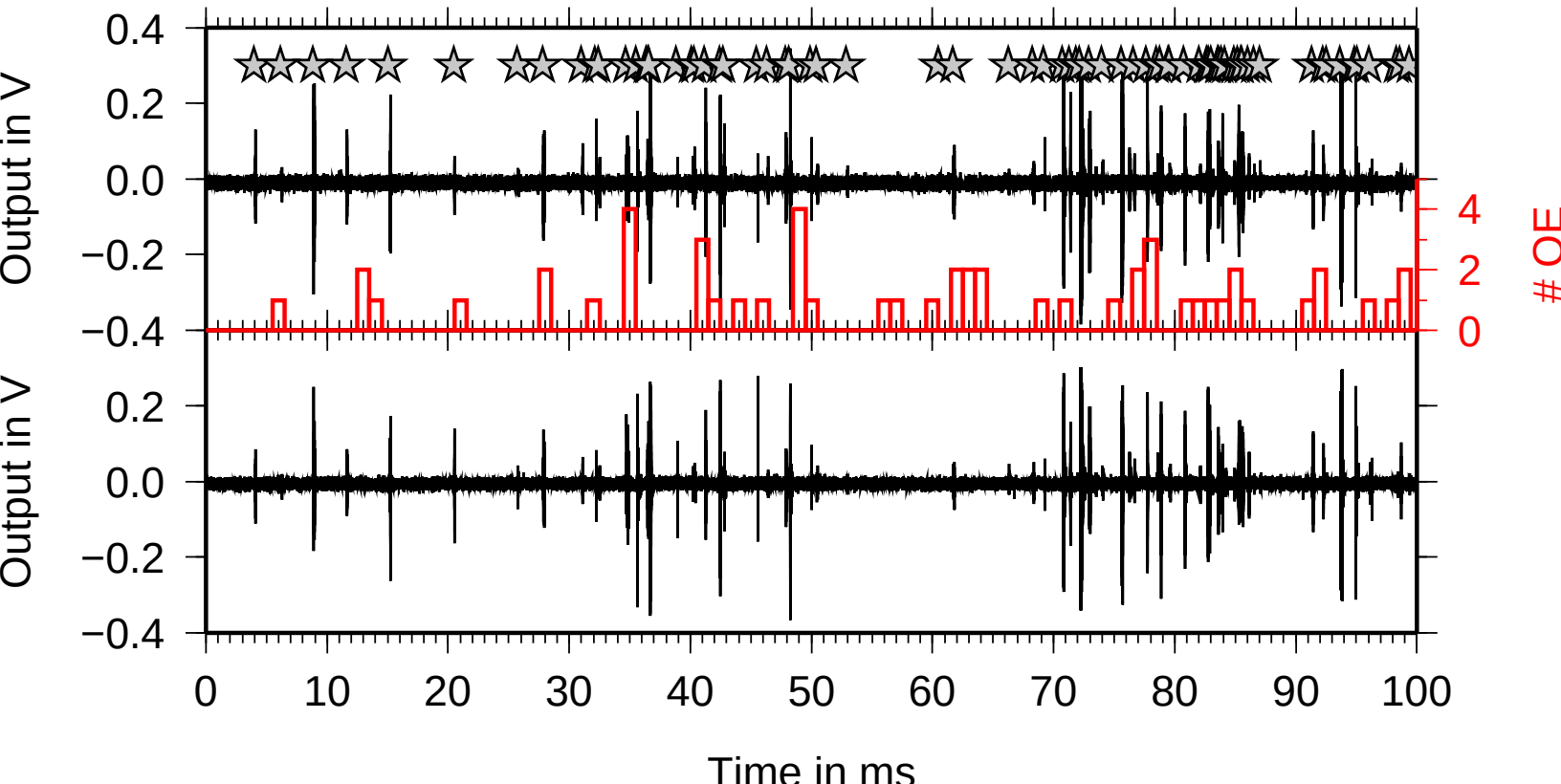

Figure 6

Click here to download Figure: fig6.eps

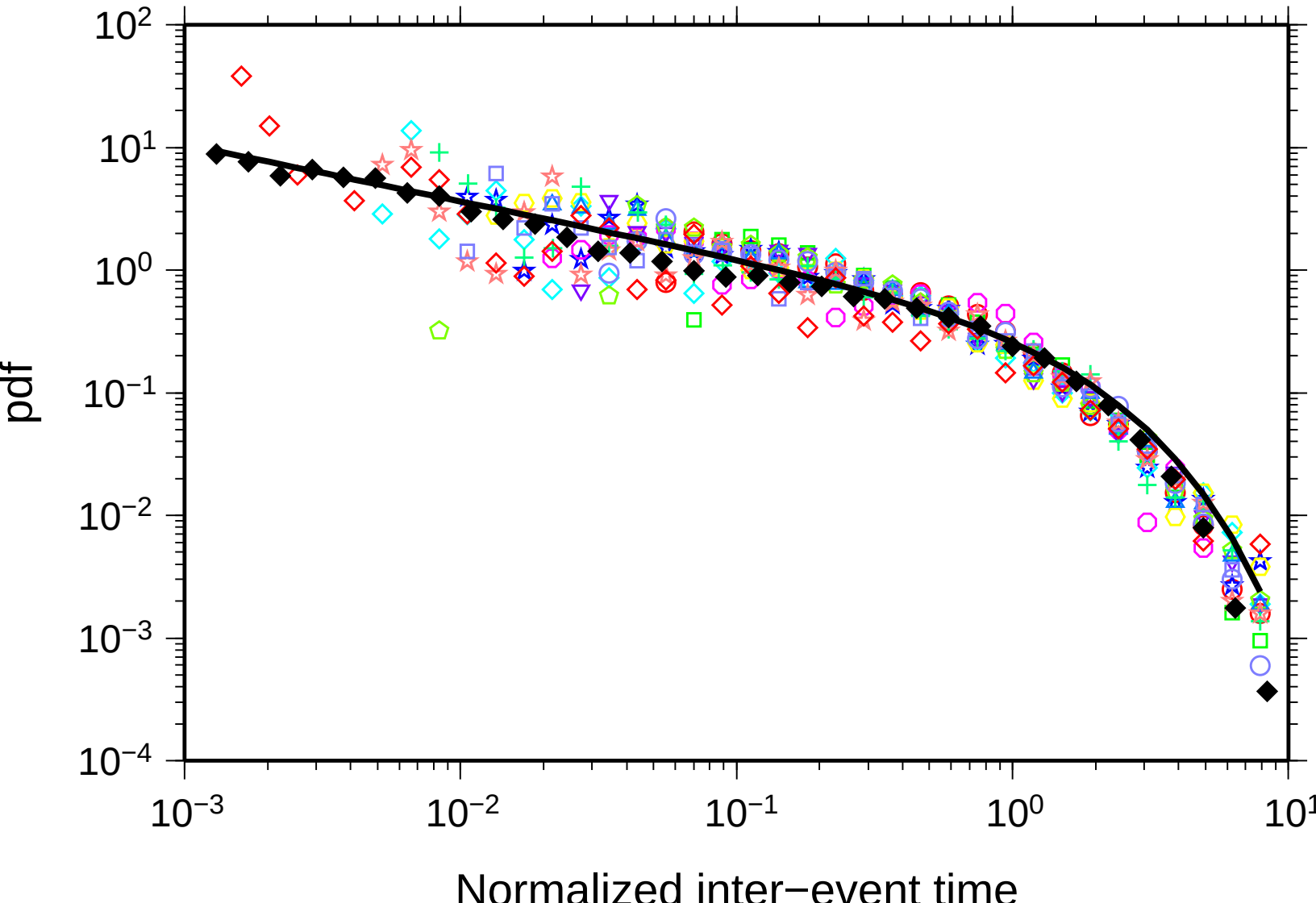

Figure 7
Click here to download Figure: fig7.eps

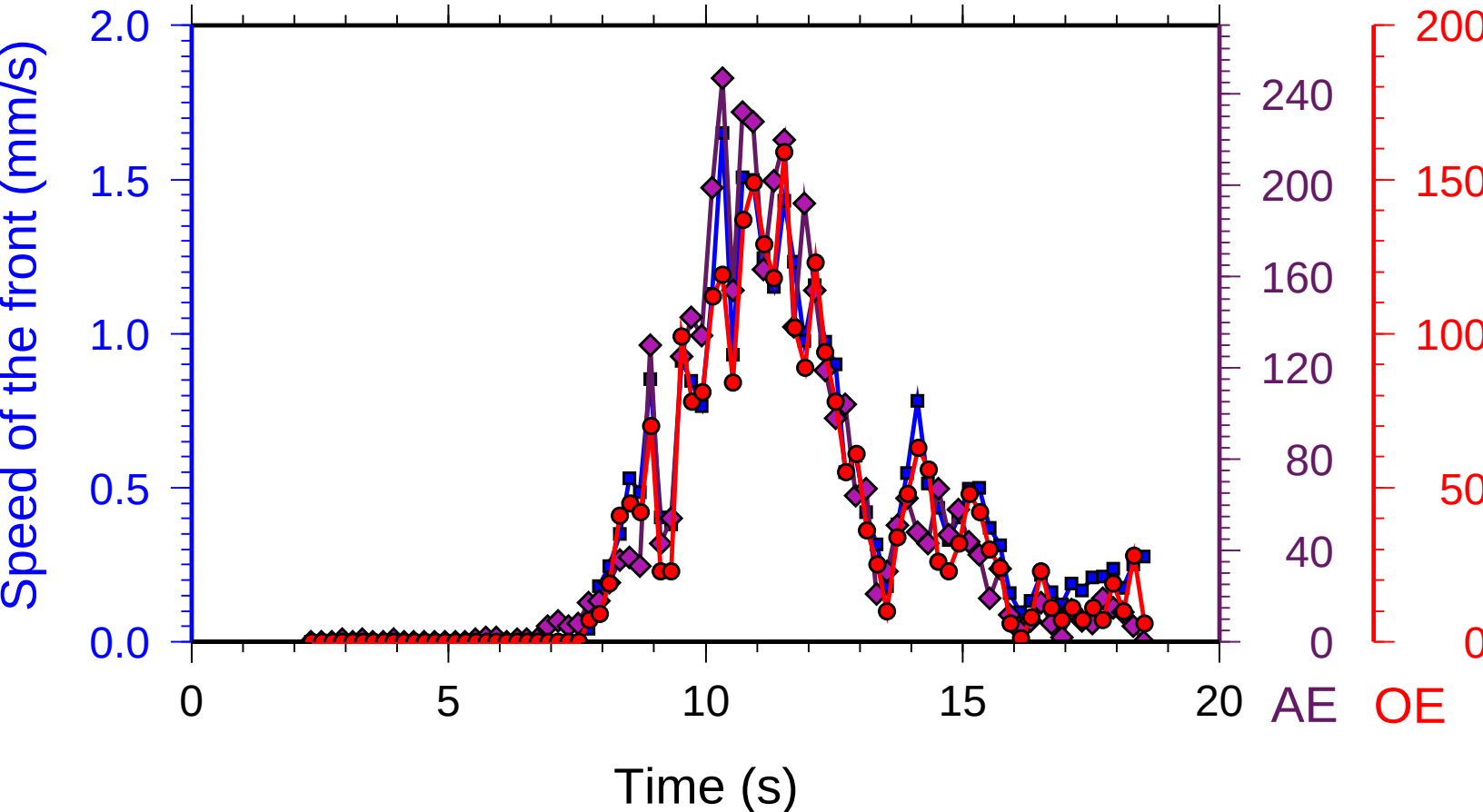

Figure 8

Click here to download Figure: fig8.eps